



# Direct Determination of Geomagnetic Baselines During Quiet Periods for Low- and Mid-Latitude Observatories

V. Haberle, A. Marchaudon, Aude Chambodut, P. -L. Blelly

## ► To cite this version:

V. Haberle, A. Marchaudon, Aude Chambodut, P. -L. Blelly. Direct Determination of Geomagnetic Baselines During Quiet Periods for Low- and Mid-Latitude Observatories. *Journal of Geophysical Research Space Physics*, 2022, 127, 10.1029/2022JA030407 . insu-03776466

HAL Id: insu-03776466

<https://insu.hal.science/insu-03776466>

Submitted on 13 Sep 2022

**HAL** is a multi-disciplinary open access archive for the deposit and dissemination of scientific research documents, whether they are published or not. The documents may come from teaching and research institutions in France or abroad, or from public or private research centers.

L'archive ouverte pluridisciplinaire **HAL**, est destinée au dépôt et à la diffusion de documents scientifiques de niveau recherche, publiés ou non, émanant des établissements d'enseignement et de recherche français ou étrangers, des laboratoires publics ou privés.



Distributed under a Creative Commons Attribution 4.0 International License



## RESEARCH ARTICLE

10.1029/2022JA030407

### Key Points:

- A basic signal filtering approach is used to determine geomagnetic baselines during quiet periods
- The baselines capture the secular variation and solar quiet current systems accurately
- The baseline method is applicable for low- and mid-latitude magnetic observatories and does not require any apriori information

### Supporting Information:

Supporting Information may be found in the online version of this article.

### Correspondence to:

V. Haberle,  
veronika.haberle@irap.omp.eu

### Citation:

Haberle, V., Marchaudon, A., Chambodut, A., & Blelly, P.-L. (2022). Direct determination of geomagnetic baselines during quiet periods for low- and mid-latitude observatories. *Journal of Geophysical Research: Space Physics*, 127, e2022JA030407. <https://doi.org/10.1029/2022JA030407>

Received 18 FEB 2022

Accepted 12 JUL 2022

## Direct Determination of Geomagnetic Baselines During Quiet Periods for Low- and Mid-Latitude Observatories

V. Haberle<sup>1,2</sup> , A. Marchaudon<sup>1</sup> , A. Chambodut<sup>2</sup> , and P.-L. Blelly<sup>1</sup>

<sup>1</sup>Institut de Recherche en Astrophysique et Planétologie, Université de Toulouse, CNRS, CNES, Toulouse, France, <sup>2</sup>Institut Terre et Environnement de Strasbourg, UMR7063, Université de Strasbourg/EOST, CNRS, Strasbourg Cedex, France

**Abstract** The geomagnetic field is composed of a variety of sources that act on a wide range of timescales and amplitudes. The separation of magnetic storm effects from quiet variations is needed to accurately quantify impacts of space weather events. The extraction of such quiet contributions within geomagnetic measurements is achieved by the determination of baselines, which, ideally, is done by a simple algorithm which captures quiet sources suitably well, while being applicable to an extensive network of magnetic observatories independent of the period of time. In this work, we apply signal filtering techniques on the horizontal components of geomagnetic field measurements from low- and mid-latitude observatories to determine baselines. The variations within the baseline are investigated for magnetically quiet periods between 1991 and 2019, focusing on long-term trends, seasonal and local time dependencies, and day-to-day variability. The analysis confirms that the contributing quiet sources include the secular variation and the solar quiet (Sq) current system. The non-negligible day-to-day variability, that is typical for Sq in low- and mid-latitudes, is embedded within the baseline. Thus, the filter approach extracts quiet magnetic field variations well. Comparisons with other baseline methods show good agreements. We conclude that the filter approach can be used to determine baselines automatically during magnetically quiet periods without the need of further apriori information and is applicable on a wide network of magnetic observatories. It marks the first step for deriving magnetic indices for (near) real-time space weather applications.

**Plain Language Summary** The Earth's intrinsic magnetic field is generated by the motion of molten rock within its interior and interacts with the constant flow of charged particles coming from the Sun. Measurements of the geomagnetic field strength on the surface not only include the intrinsic magnetic field but also phenomena that arise due to this interaction. Some of these phenomena show regular variations without major effects and some, like solar storms, are able to disrupt the geomagnetic field, affecting technological systems. In order to quantify how harmful disruptive events are, it is important to determine the regular variations first. In this paper, we determine the regular variations within the signal (baselines) by applying signal filtering techniques on geomagnetic field measurements. Our analysis shows that regular variations during undisturbed days in low- and mid-latitude ranges are captured accurately.

### 1. Introduction

Ground magnetic observatories continuously monitor the evolution of Earth's magnetic field, producing high quality magnetic field measurements at stable locations. These measurements display a high degree of variability as the geomagnetic field is a superposition of various sources spanning a wide amplitude-frequency spectrum (Constable & Constable, 2004). These sources can operate on overlapping frequencies and their spatial and temporal separation is an active field of research requiring sophisticated modeling techniques (Wardinski & Thébault, 2019, and references therein). Internal sources comprise the main field that is generated within the fluid outer core by geodynamo processes; the lithospheric field as a result of the superposition of induced and remnant magnetisation of the Earth's sub-surface rocks; and the oceanic circulation, tidal and induction effects. The most prominent temporal feature of the internal part is the variation of the main field, the so-called secular variation, noticeable over periods exceeding a month. The main magnetic field accounts for over 93% of the magnetic field measured at the Earth's surface. The rest may be attributed to external sources with origins in the magnetosphere and ionosphere which temporal variations range from shorter than a few seconds to decades (Finlay et al., 2017). Among them, the Sun with its solar cycle induces variations with periods of around 11 years, as well as periods of 27 days due to its rotation (Kunagu et al., 2013; Ma et al., 2012; Shinbori et al., 2014). Disturbance events like solar flares and coronal mass ejections that hit Earth's magnetic field are able to induce sudden changes, within

©2022. The Authors.

This is an open access article under the terms of the Creative Commons Attribution License, which permits use, distribution and reproduction in any medium, provided the original work is properly cited.

minutes to days, reaching relatively high amplitudes of over 100 nT within geomagnetic field measurements at low-to mid-latitudes (Cliver & Dietrich, 2013; Kozyreva et al., 2018). On days with no significant external influences, known as quiet days, the magnetic field, measured at a stable location on Earth's surface, features daily variations in the sense of a smooth curve. These variations have distinct contributions with periods of 24, 12, 8 and 6 hr (Campbell, 2003) and are mainly associated with the solar quiet ( $S_q$ ) current systems at mid-latitudes. These systems feature two current cells, one in the northern hemisphere (NH) flowing anti-clockwise and one in the southern hemisphere (SH) flowing clockwise within the sunlit ionospheric dynamo region which are the result of ionisation by solar radiation (Campbell, 1989). They show peculiar seasonal and local time dependencies, being most intense during summer months in mid-latitudinal regions and reaching lowest amplitudes during the night when irradiation ceases (Hitchman et al., 1998; Shinbori et al., 2017; Takeda, 1999; Yamazaki & Maute, 2016).

Thus, magnetic field measurements are a rich source of information on various physical phenomena and processes affecting Earth. An important application of magnetic observatory measurements is the derivation of magnetic indices which quantify the overall geomagnetic activity or idealised physical processes like ionospheric and magnetospheric current systems (see Menvielle et al. (2011) for a comprehensive review). The three indices  $K_p$ ,  $aa$  and  $am$  are sub-auroral magnetic activity indices endorsed by IAGA, the International Association of Geomagnetism and Aeronomy (<https://www.iaga-aiga.org/>). These indices rely on intermediate data-products of magnetic observatory time series, the so-called  $K$ -indices, having a temporal resolution of 3 hr. One of the main challenges when deriving magnetic indices is to separate the contributions of relevant sources from the rest of the magnetic field signal in an effective and timely manner. Generally, this is achieved by determining a so-called “baseline” which is extracted from the measurements. This definition of “baseline” is used throughout the present paper. As such, it should not be confused with the baseline used in other contexts, for example, in the calibration of magnetic observatory data. The first qualitative description of a baseline was given by Bartels et al. (1939) who defined it as a smooth and to-be-expected curve during a magnetically quiet day. At this epoch, its derivation included hand-scaling of such regular daily variation curves as identified by trained observers. Mayaud (1967) concretised this description to rules which act as guidelines. With the raise of the digital age and the increasing availability of magnetic data, the need for automatic determination of baselines has become imperative. In 1991, IAGA endorsed four algorithms to automatically determine the quiet baseline for  $K$ -indices (Menvielle et al., 1995) which includes the Finnish Meteorological Institute (FMI) method (Sucksdorff et al., 1991). The FMI method uses the observatory's magnetic latitude as input to derive baselines. The main geomagnetic field changes over time, thus magnetic coordinates evolve. They have to be calculated and adjusted following the time frame of availability of the international reference model (IGRF updated every 5-years).

With the potential of improvement given by data accessibility, many other techniques and methodologies have been developed during the past years. Some prominent examples include the baseline calculation for the PC index as introduced by Janzhura and Troshichev (2008), the method used by the International Monitor for Aurora Geomagnetic Effects (IMAGE) as described by Van De Kamp (2013) and the one used by SuperMAG as described by Gjerloev (2012).

In this paper, we introduce a direct and easily reproducible method to determine such magnetic field baselines for ground magnetic observatory measurements. It is based on fundamental signal treatment techniques and we investigate its applicability to produce baselines between 1991 and 2019. We limit our study to magnetic observatories located at low- and mid-latitudes and present physical analysis and interpretation of contributing sources during magnetically quiet periods.

The geomagnetic field data and derivation of the baselines are described in Section 2. Section 3 analyses observed variations within the different frequency regimes, which are related to physical phenomena during magnetically quiet periods in Section 4. Section 5 demonstrates the baseline and compares it to other methods, followed by the conclusion (Section 6).

## 2. Data

Vectorial geomagnetic field measurements from magnetic observatories between 1991 and 2019, covering more than two solar cycles, are used. The measurements have a temporal resolution of 1 min, that is, one day comprises 1440 data points. They are made available through the International Real-time Magnetic Observatory

**Table 1**  
*Finite Impulse Response (FIR) Filters, Corresponding Passing Frequencies and Their Notation*

Signal contribution	Pass frequencies	Notation	
Long-term	below $7.716 \times 10^{-6}$ Hz	$x_{>24}$	$y_{>24}$
Diurnal	$7.716 \times 10^{-6}$ – $1.1574 \times 10^{-5}$ Hz	$x_{24}$	$y_{24}$
Semi-diurnal	$1.1574 \times 10^{-5}$ – $2.3148 \times 10^{-5}$ Hz	$x_{12}$	$y_{12}$
8 hr	$2.3148 \times 10^{-5}$ – $3.4722 \times 10^{-5}$ Hz	$x_8$	$y_8$
6 hr	$3.4722 \times 10^{-5}$ – $4.6296 \times 10^{-5}$ Hz	$x_6$	$y_6$

*Note.* The sum of the five filter outputs forms the baselines  $x_B$  and  $y_B$ .

Network (INTERMAGNET, <https://intermagnet.github.io/>) data repository which ensures high quality data with consistent observing practices regarding modern standard specifications for measurement procedures and recording equipment. The use of definitive data, that is, fully calibrated magnetic observatory data, rather than variational data issued from direct outputs of instruments, allows to fully assess the magnitude of the various contributions and to take advantage of the homogeneous and continuous time series.

In the following, we consider the horizontal components of the magnetic field in the local spherical frame, namely  $X$  towards the geographic North and  $Y$  towards the geographic East ( $H$  being the intensity of the magnetic field in the horizontal plane, i.e.,  $H = \sqrt{X^2 + Y^2}$ ). We concentrate on observatories in regions with magnetic latitudes between  $\pm 10^\circ$  and  $\pm 60^\circ$  in eccentric dipole coordinates (Laundal & Richmond, 2016). This constraint allows to mitigate influences from equatorial and auroral electrojets at equatorial and high magnetic latitudes.

To illustrate our results, we primarily use data from the magnetic observatory Chambon-la-Forêt (CLF) located in France, Europe, with geographic latitude  $48.025^\circ$ . It is located in mid-latitudes and can thus be considered a representative example. Other observatories are used when applicable.

A list of all used observatories (location and used data) is enclosed as Supporting Information S1.

## 2.1. Baseline Derivation

Magnetic field measurements may be viewed as discrete time signals consisting of the superposition of various sources. In order to extract specific frequency contributions, a finite impulse response (FIR) filter is applied. For the truncation, we make use of the Hamming window function to smooth the convolution operation in the frequency domain with a window-size of 3 days, that is, 3 days correspond to 4320 min/data-points. These filtering techniques and window functions are standard tools in signal processing described in corresponding books, for example, Proakis and Manolakis (2006). Similar numerical filters have been used to remove diurnal components from ground magnetic measurements, see for example, Behannon and Ness (1966a); Behannon and Ness (1966b); Ness and Williams (1966); Bhargava and Yacob (1970); Jadhav et al. (2002).

The main contributions to the quiet daily variations are to be found within the periods of 24, 12, 8 and 6 hr in low- and mid-latitudinal regions. Additionally to these (sub-) diurnal variations, a smooth change of the geomagnetic field is induced by sources acting above the 24 hr timescales (like the secular variation). These considerations result in a total of five filters. To extract long-term variations, we use a low-pass filter with cut-off frequency of  $7.716 \times 10^{-6}$  Hz corresponding to variations above 36 hr within the signal. For the four (sub-) diurnal frequencies, we eventually use band-pass filters that are implemented with the help of low-pass filters. To extract the 24-hr variations, we apply a low-pass filter with cut-off frequency of  $1/24\text{hr} = 1.1574 \times 10^{-5}$  Hz on the signal, from which we subtract the output of the long-term filter. The 12-hr variations are then computed as the difference between the low-pass filter with cut-off frequency of  $1/12\text{hr} = 2.3148 \times 10^{-5}$  Hz applied on the signal and the sum of the outputs of the 24 hr band-pass and the long-term filter. The 8 and 6 hr band-pass filters are implemented analogously. The filters are applied to the horizontal components  $X$  and  $Y$  of the geomagnetic field measurements. In the following, we label the magnetic observatory measurements in capital  $X$ ,  $Y$ , and the filter outputs in lower-case  $x$ ,  $y$  with the corresponding period range as subscript, as summarised in Table 1. The sources of the quiet geomagnetic field superpose each other and accordingly the baseline per component is defined as the sum of the five filter outputs, that is, the baseline for  $X$  is  $x_B = x_{>24} + x_{24} + x_{12} + x_8 + x_6$  and for  $Y$  is  $y_B = y_{>24} + y_{24} + y_{12} + y_8 + y_6$ . These baselines are direct filter outputs and thus totally independent of any apriori information regarding the position of the considered magnetic observatory or of the local time. Figure 1 shows an example of the decomposition of  $X$  and  $Y$  from CLF by each of the filters in the five upper panels. The baseline is demonstrated in the sixth panel (in red) plotted together with the measurements (in black). The residuals are calculated as the difference between the magnetic observatory measurements and the defined baseline, visualised in the bottom panel.

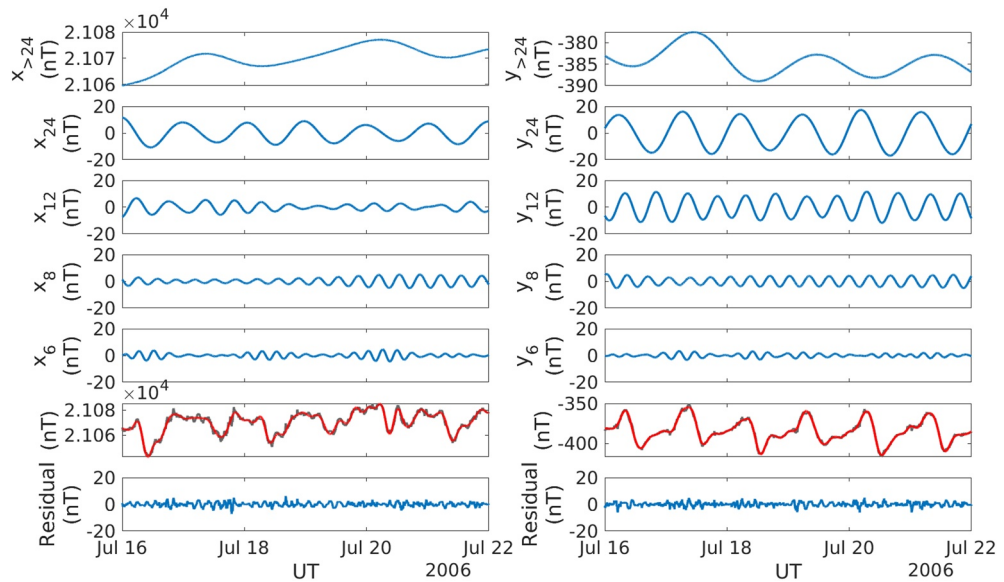


**Figure 1.** Decomposition of  $X$  (left) and  $Y$  (right) measurements at Chambon-la-Forêt over 6 quiet days. From top to bottom: the five consecutive finite impulse response filters; comparison of measured magnetic field component (black) with the determined quiet baseline (red); residuals calculated as difference between measurements and baseline.

## 2.2. Selection of Magnetically Quiet Days

In order to understand which quiet sources are contained within our filter baseline, we have to study its variations during geomagnetically quiet periods. Therefore, we select time intervals for which the contribution of disturbance events from external sources like geomagnetic storms is minimised. To do so, we need to use an independent indicator regarding the quietness of the considered days. The quietest CK-days (“Really Quiet (C)” and “Quiet (K)”, [http://isgi.unistra.fr/events\\_ckdays.php](http://isgi.unistra.fr/events_ckdays.php)) are IAGA-endorsed data products provided by the International Service of Geomagnetic Indices (ISGI, <http://isgi.unistra.fr/>). They indicate magnetically quietest days by using the  $aa$  index (Mayaud, 1972), with a mean lower than 13 nT. Two data products exist: the quietest days over 24-hr (CK24) and over 48-hr (CK48) centered on the UT day. We thus choose the CK48 days in order to be as strict as possible in ensuring the minimisation of external disturbance contributions within the magnetic field measurements. Indeed, between 1991 and 2019, there is a total of 3040 CK48 days. The amount of quiet days per year is not evenly distributed (see bottom panel of Figure 2) and clearly anti-correlated with solar activity (top panel). To quantify solar cycle and solar activity, we use the well defined daily F10.7 index, measured in solar flux units (sfu), see Tapping (2013) for an overview.

In order to understand which quiet sources are contained within our filter baseline, we have to study its variations during geomagnetically quiet periods. Therefore, we select time intervals for which the contribution of disturbance events from external sources like geomagnetic storms is minimised. To do so, we need to use an independent indicator regarding the quietness of the considered days. The quietest CK-days (“Really Quiet (C)” and “Quiet (K)”, [http://isgi.unistra.fr/events\\_ckdays.php](http://isgi.unistra.fr/events_ckdays.php)) are IAGA-endorsed data products provided by the International Service of Geomagnetic Indices (ISGI, <http://isgi.unistra.fr/>). They indicate magnetically quietest days by using the  $aa$  index (Mayaud, 1972), with a mean lower than 13 nT. Two data products exist: the quietest days over 24-hr (CK24) and over 48-hr (CK48) centered on the UT day. We thus choose the CK48 days in order to be as strict as possible in ensuring the minimisation of external disturbance contributions within the magnetic field measurements. Indeed, between 1991 and 2019, there is a total of 3040 CK48 days. The amount of quiet days per year is not evenly distributed (see bottom panel of Figure 2) and clearly anti-correlated with solar activity (top panel). To quantify solar cycle and solar activity, we use the well defined daily F10.7 index, measured in solar flux units (sfu), see Tapping (2013) for an overview.

## 3. Variations of the Filter Outputs

In this section, we first present the filter outputs during the entire considered period, revealing their global variations. These results lead us to deeper investigate the variations within the combined daily filter outputs during magnetically quiet periods only.

### 3.1. Filter Outputs

#### 3.1.1. Long-Term Filters

The long-term filters preserve all contributions with periods above 36 hr. Their outputs  $x_{>24}$  and  $y_{>24}$  are shown in Figure 3 for CLF. The upper panels show variations over 29 years (1991–2019), whereas the lower panels focus on a three month period (October–December 2007) comparing long-term filters (blue) with the magnetic observatory measurements  $X$ ,  $Y$  (grey). The

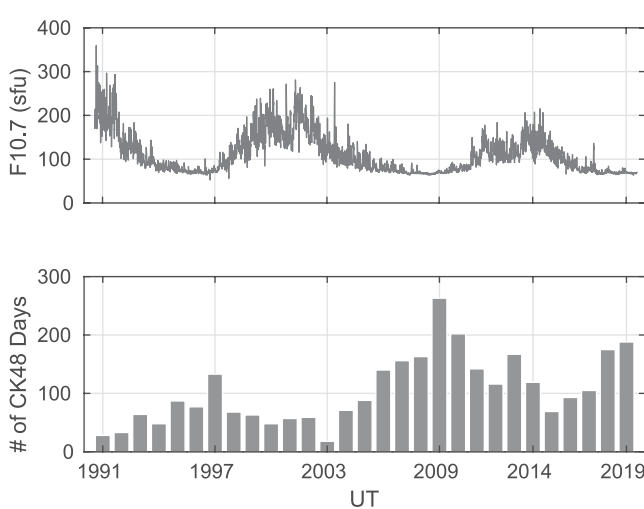


**Figure 2.** Solar activity and quiet days between 1991 and 2019. The upper panel depicts the F10.7 daily values in solar flux units, while the lower panel indicates the amount of magnetically really quiet (CK48) days per year.

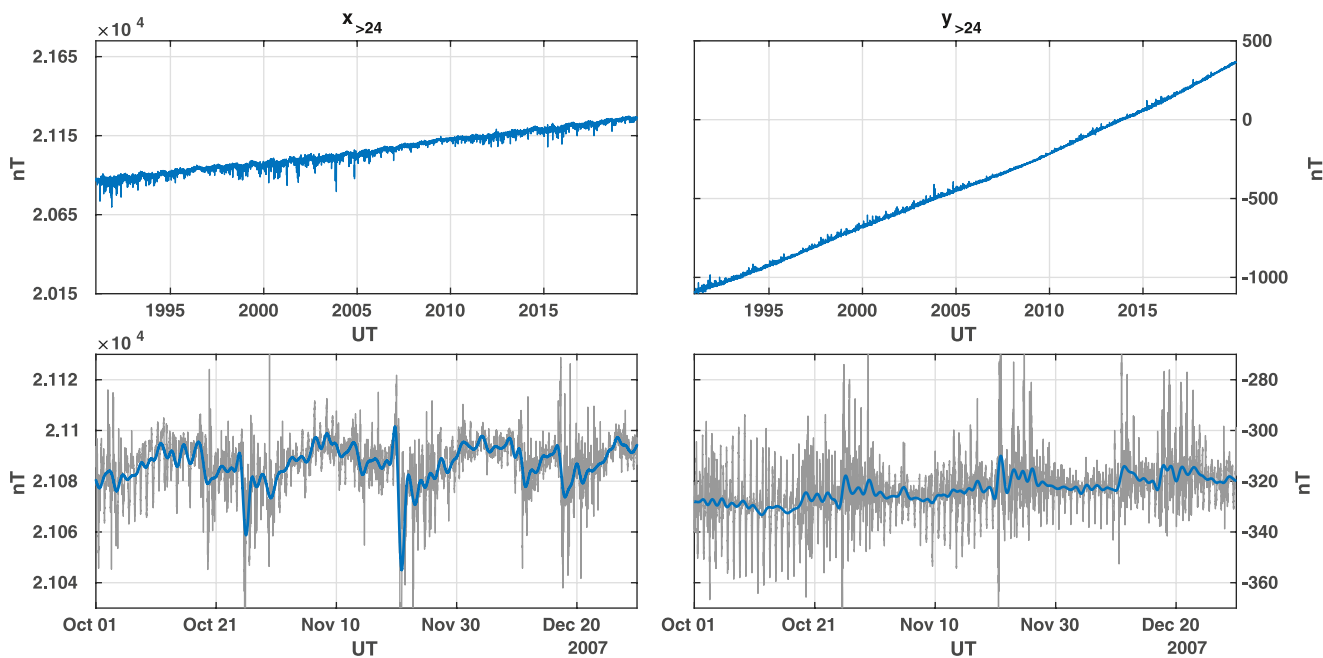


**Figure 3.** Variations within the long-term contributions  $x_{>24}$  (left panels) and  $y_{>24}$  (right panels) in blue for Chambon-la-Forêt. Upper panels demonstrate the long-term trend over 29 years, while the lower panels present a zoomed-in view of 3 months whereby the magnetic components  $X$ ,  $Y$  are indicated in grey.

upper left panel shows a steady increase in  $x_{>24}$  of about 570 nT, with shorter fluctuations of up to 300 nT during the considered time-interval. Similarly, the right upper panel shows a steady, but steeper increase of  $y_{>24}$  (around 1500 nT), transitioning from negative to positive values around 2014, with shorter fluctuations in the order of tens of nanotesla. The lower panels illustrate variations in the 27-days regime which are very clear for  $x_{>24}$  and less clear, but still present, for  $y_{>24}$ . Physical processes that are responsible for these variations are discussed in Section 4.1.

### 3.1.2. 24h, 12h, 8h and 6h Filters

In this subsection, we look at the global patterns of the 24, 12, 8 and 6 hr filter outputs of the  $X$  and  $Y$  components at CLF and the combined daily signal containing the sum of the four filter outputs:  $x_D = x_{24} + x_{12} + x_8 + x_6$  and  $y_D = y_{24} + y_{12} + y_8 + y_6$ . They are presented in Figures 4 and 5 with respect to local time and day of year, alongside the F10.7 index to facilitate comparisons with solar cycle phases. For demonstration purposes, we illustrate dependencies on local time, season and solar activity corresponding to variable solar irradiation conditions over approximately one solar cycle between 2000 and 2012. The analog figures for the entire period 1991–2019 can be found in Supporting Information S1.

We first focus on the individual filter outputs which are presented in the four central panels of Figure 4 for  $X$  and of Figure 5 for  $Y$ . Comparisons to F10.7 (top panels) show that the level of magnetic activity of each filter output, especially the 24 hr ones, is higher during the maximum phase of the solar cycle. Periodical patterns can be observed with respect to day-of-year and, more specifically, season and local time with diurnal, semi-diurnal, 8 and 6 hr recurrence for each individual filter output. These patterns can be disturbed from 1 day to the other by magnetospheric processes enhancing the level of magnetic activity, especially during the maximum of the solar cycle. Finally, the filter outputs contributing to the  $X$  component are in general twice as less intense as the ones contributing to the  $Y$  component. More specifically, for the  $X$  component, the 24 hr filter is by far the most intense, the 12, 8 and 6 hr filter contributions being secondary, while for the  $Y$  component the 24 and 12 hr filters are more comparable in intensity.

Second, we look at the combined daily signals  $x_D$  and  $y_D$  presented in the lowest panels of Figures 4 and 5. Similar to the individual filter outputs,  $y_D$  is twice as intense as  $x_D$ . For both, the periodical patterns remain clear and highlight solar cycle, seasonal and daily variations with enhanced activity during solar maximum (around 2002), summer periods and daylight hours.  $x_D$  has a seasonal-dependent minimum around local noon which is surrounded

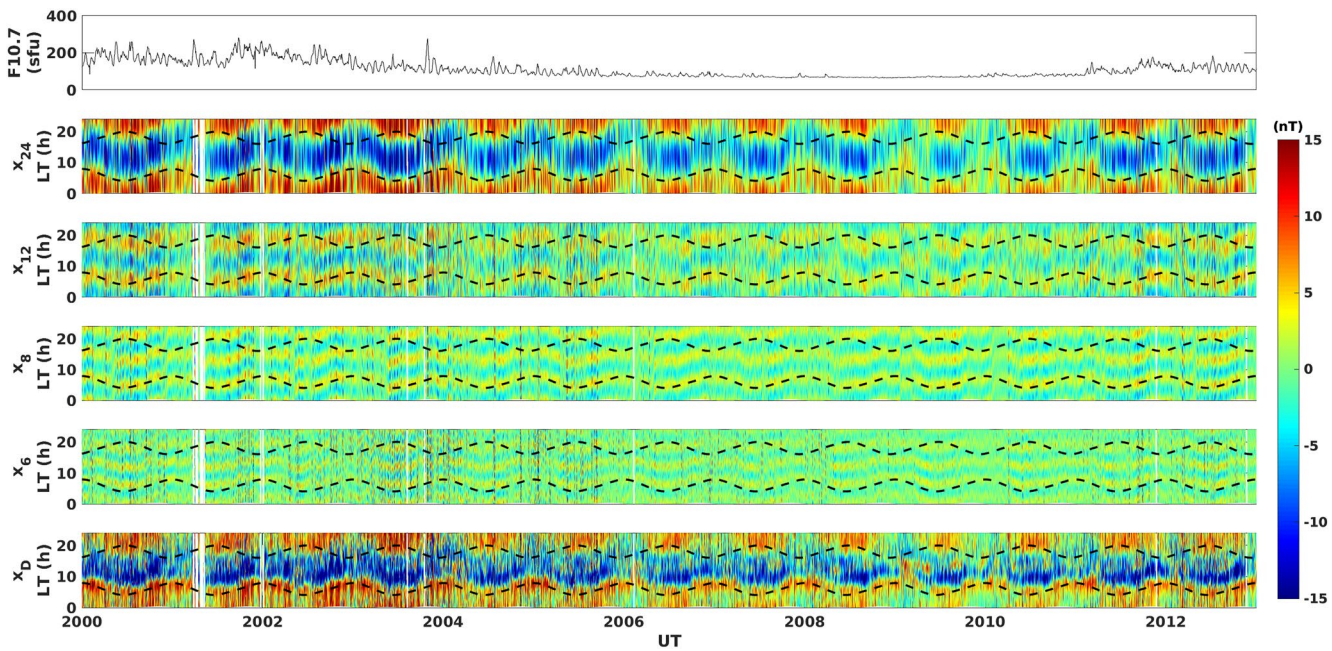


**Figure 4.** Filter outputs between 2000 and 2012 as function of solar local time (LT) for the X component of Chambon-la-Forêt. From top to bottom: the F10.7 daily values in solar flux units;  $x_{24}$ ;  $x_{12}$ ;  $x_8$ ;  $x_6$  and  $x_D$  in nT. Dashed black lines indicate local time for sunrise (morning hours) and sunset (evening hours). Periods with unavailable data are not represented and appear as white vertical stripes. Note that the limits of the colour-scale range from  $-15$  to  $15$  nT.

by two positive crests of activity around dawn and dusk (at least during summer).  $y_D$  has a maximum followed by a minimum of activity, with the zero-crossing centred around local noon, which shows no clear dependency on season. We superimposed the occurrence of sunrise and sunset at 110 km altitude on corresponding panels in Figures 4 and 5 (black dashed lines). The activity increase is well phased with sunrise for both combined signals, while the activity decrease is more complex to associate with sunset. A clear reduction of the activity is observed in the night time for  $y_D$  where it almost reaches zero, implying that all filter outputs added together cancel out,

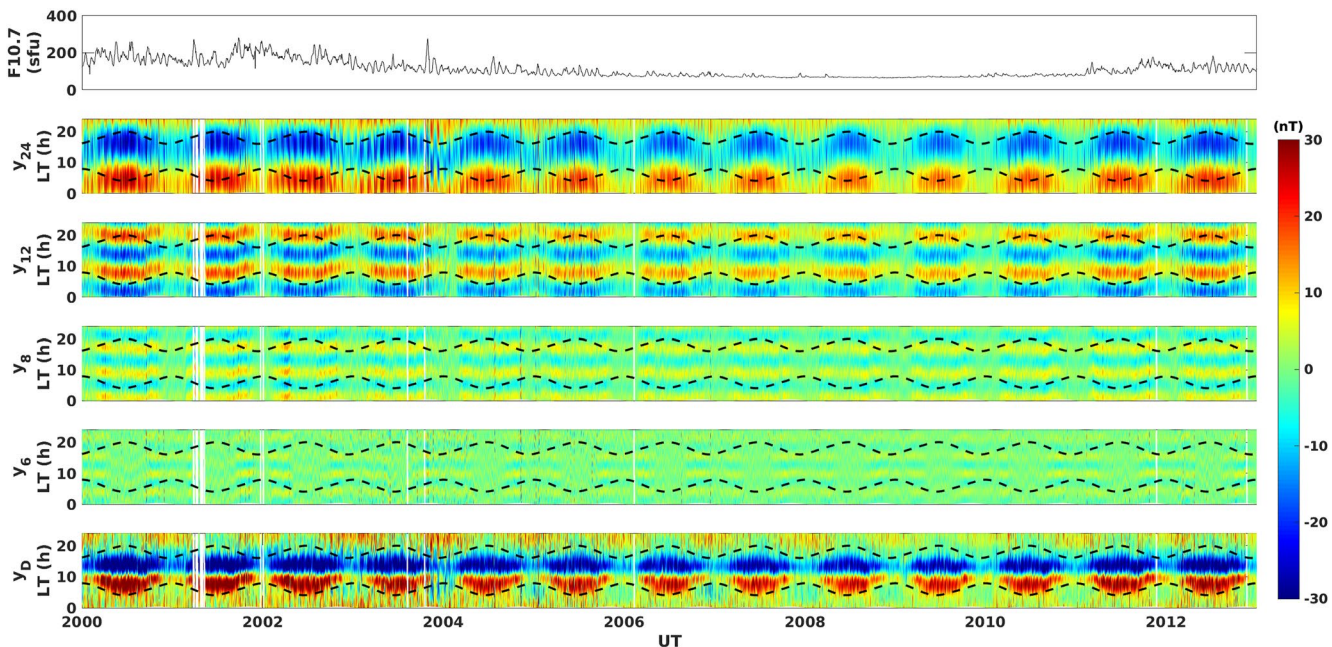


**Figure 5.** Analog to Figure 4 for the Y component of Chambon-la-Forêt. Note that the limits of the colour-scale range from  $-30$  to  $30$  nT.

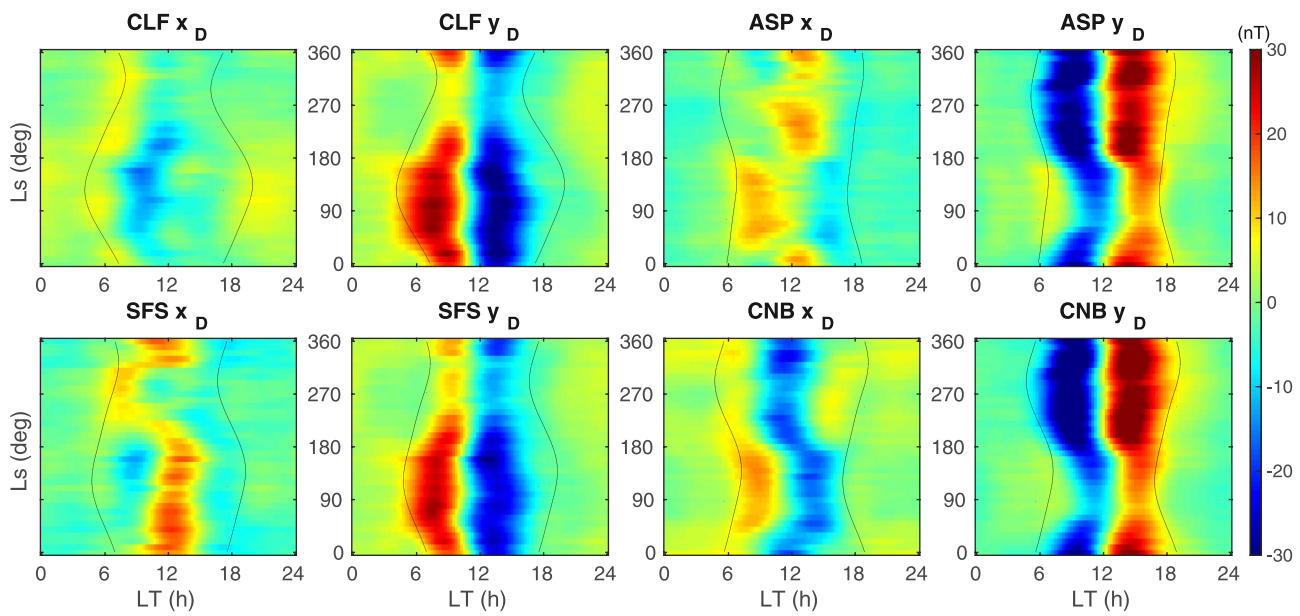


**Figure 6.** Super-posed epoch analysis of the combined signals  $x_D$  and  $y_D$ , depending on local time and season for two European observatories (CLF, SFS) and two Australian observatories (ASP, CNB), during magnetically quiet days. Black lines indicate local sunrise (morning hours) and sunset (evening hours). Note that the colour-scale is the same for all panels.

showing that only the combination of the individual filters is physically meaningful. The combined signal  $x_D$  still displays night-side activity especially during solar maximum, but also in summer nights during solar minimum.

### 3.2. Variations of the Combined Daily Filters During Magnetically Quiet Periods

The previous section showed a clear trend within the long-term filters that follows secular variation (see Section 4.1). There are evident dependencies of the combined daily filters on season and local time. However, all filter outputs also contain obvious storm signatures which potentially mask out the quiet magnetic variations. As we would like to better understand the quiet sources that contribute to the combined daily filters, we need to avoid storm signatures as much as possible and thus, we constrain the following analysis to magnetically quiet periods only.

#### 3.2.1. Seasonal and Local Time Patterns

To gain a better understanding of the variations within the combined daily filter outputs, we focus on their local time and seasonal dependencies. We show examples for several observatories at low and mid-latitudes, where the signatures of equatorial and auroral electrojets are minimized, and during magnetically quiet periods as defined in Section 2.2. Per magnetic observatory, we conduct a super-posed epoch analysis (SEA) of  $x_D$  and  $y_D$  in dependence of solar local time and day of year (season) for CK48 days between 1991 and 2019 (see Figure 2). The season can be described by the solar longitude  $L_s \in (0^\circ, 360^\circ)$  which is derived from the position of Earth around the Sun, whereby  $L_s = 0^\circ$  defines spring equinox in the NH. The data is arranged into bins of  $\Delta L_s = 10^\circ$  (vertical axis) and  $\Delta LT = 10$  min (horizontal axis). The value per bin is derived as the average of all values that belong to the specific bin. Here we present four representative stations in detail. The SEA of further stations may be found in Supporting Information S1. The selection of specific observatories presented in this study is motivated by the need to examine the baseline properties in both hemispheres and in different geographic sectors while ensuring that the length of considered time series is sufficient to produce meaningful statistics. The period for which data is available at each observatory can be found in Supporting Information S1. Nevertheless, an exhaustive examination of the baselines obtained shows consistent results, indicating that the filtering method is applicable for all INTERMAGNET observatories at low and mid-latitudes.

Figure 6 presents the resulting SEA for two European observatories: CLF and San Fernando (SFS), and two Australian observatories: Alice Springs (ASP) and Canberra (CNB). Note that they are located in latitude from

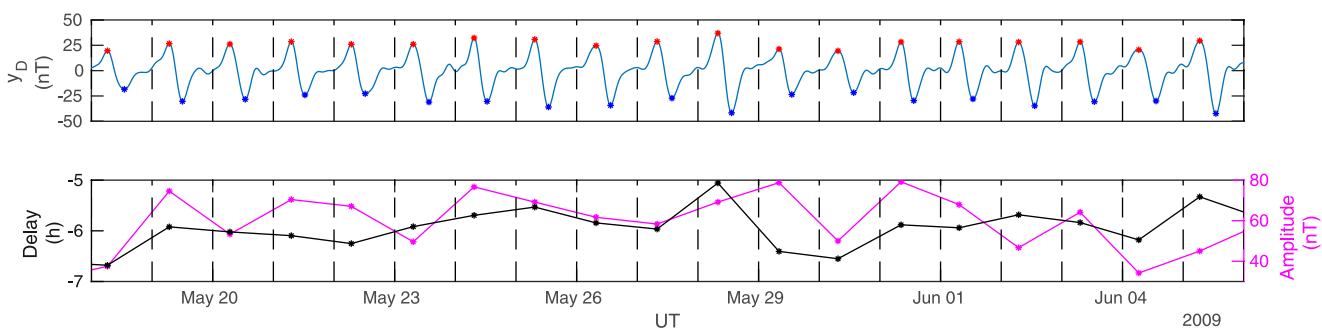


**Figure 7.** Day-to-day variability of  $y_D$  at Chambon-la-Forêt. The upper panel depicts the daily evolution of  $y_D$  (blue) with daily maximum/minimum marked by red/blue dots. The lower panel presents the variations in delay (black) and amplitude (magenta) between maxima and consecutive minima.

North to South in this order. The black lines indicate the mean local sunrise (morning hours) and sunset (evening hours) at an altitude of 110 km between 1991 and 2019. The upper left panels show the SEA for CLF. The combined filter output  $y_D$  describes a maximum during morning and a minimum during afternoon hours, almost vanishing during night times throughout the year. The increase in activity during morning hours strictly follows local sunrise, appearing earlier during summer than during winter, while the activity decreases rather constantly in the afternoon around 15 hr LT, except during winter solstice. In addition to the prolonged activity, the signal intensity is stronger during summer (in NH  $L_s = 90^\circ$ ) than during winter (in NH  $L_s = 270^\circ$ ). One of the most striking features is the relatively constant zero-crossing of the activity around noon for  $y_D$ . The pattern of  $x_D$  is less clear. As noted in the global patterns before, the dawn crest of activity is well phased with sunrise and is present throughout the solar longitude, while the minimum and the dusk crest that extends into the pre-midnight hours, are mainly observed during summer and autumn.

SFS is located South of CLF and its SEA is presented in the lower left panels of Figure 6. Its  $y_D$  shows a remarkably similar pattern as CLF, being well phased with sunrise and to a lesser extent with sunset. The main difference to CLF lies within its  $x_D$  which describes a maximum around local noon from spring to autumn. Around autumn equinox ( $L_s = 180^\circ$ ), the maximum abruptly shifts to morning hours and returns to noon hours shortly after winter solstice ( $L_s = 270^\circ$ ). On the other hand, no clear activity is observed during night, at dawn, or at dusk and only a rather limited minimum is observed after dawn during summer.

The solar longitude describes the season reversely in each hemisphere, for example, summer in SH is at  $L_s = 270^\circ$  and winter at  $L_s = 90^\circ$ . ASP is located in the SH and its SEA is presented in the top right panels of Figure 6. The combined signal  $y_D$  describes a minimum in the morning hours and a maximum during afternoon hours, as opposed to NH stations, with stronger amplitudes during summer. As for NH observatories,  $y_D$  is well phased with sunrise and additionally with sunset. The only exception is during winter at sunrise, when a local and fainter maximum can be observed. The combined signal  $x_D$  is not as clearly phased with sunrise. During spring ( $L_s = 180^\circ$ ) and autumn equinox ( $L_s = 0^\circ$ ),  $x_D$  shows a maximum around noon. Similar to SFS in the NH, the maximum shifts to morning hours shortly after autumn equinox and returns to noon hours at spring equinox.

CNB is situated south of ASP and analogously shows a remarkably similar behaviour in  $y_D$ .  $x_D$  has a minimum during day-light hours that shifts to later LT between autumn and spring equinox. During local winter,  $x_D$  shows also a local maximum in the morning hours.

These global patterns may be interpreted as magnetic footprints of current cells flowing anti-clockwise in the NH and clockwise in the SH, following the apparent motion of the sun. The focus would be located between CLF and ASP for the northern cell and between CNB and ASP for the southern one. More physical interpretation of these results are given in subsection 4.2.

### 3.2.2. Day-To-Day Variability

The combined filter outputs  $x_D$  and  $y_D$  not only vary on seasonal timescales but also on a day-to-day basis, even during quiet periods. This behaviour can be followed on the top panel of Figure 7 where CLF's  $y_D$  is plotted over consecutive CK48 days during summer 2009. We see a recurrent sinusoidal pattern during sunlit hours which amplitude and occurrence times of maxima (red stars) and minima (blue stars) vary from one day to the other.

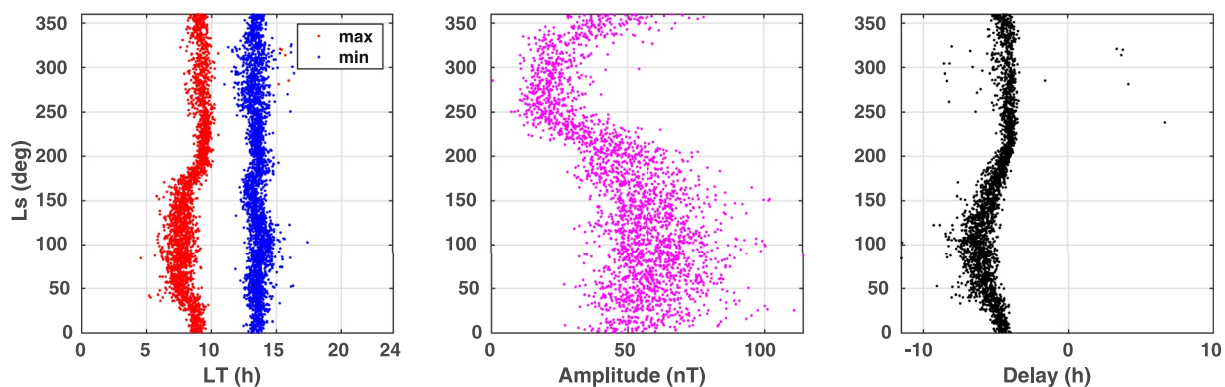


**Figure 8.** Statistics of seasonal and day-to-day variability of  $y_D$  at Chambon-la-Forêt during quiet days between 1991 and 2019. From left to right, the panels show local time occurrence of extrema, amplitude and delay between them.

To illustrate this variability quantitatively, we first determine the local time occurrence of the maximum and minimum for each day during sunlit hours. Then, the amplitude is derived as the difference between the values at maximum and at the consecutive minimum (given in nanoteslas) and finally, the delay is given as the time in hours that has passed to reach the consecutive minimum from the maximum. The bottom panel of Figure 7 illustrates these amplitudes (magenta) and delays (black) from 1 day to the next. The amplitude varies significantly on a daily basis between 20 and 80 nT, as does the delay between 5 and 8 hr in this example.

We compute the day-to-day parameters, that is, the occurrence times of extrema, peak-to-peak amplitudes and delays, for  $y_D$  at CLF for all quiet days between 1991 and 2019. They are presented as a scatter-plot against solar longitude in Figure 8 and from which it is clear that the day-to-day variability has a strong seasonal dependency. For the maximum, two regimes can be distinguished: during summer months the maxima occur around 06–09 hr LT, while they occur later at around 09–10 hr LT during winter, which is directly related to the LT sunrise shift with season as already seen in the previous section. The transition between these two regimes happens abruptly around  $L_s = 10^\circ$  and  $L_s = 180^\circ$ . On the other hand, the timing of the minimum is more constant over time, which, too, is related to the decrease of activity observed constantly around 15 hr LT in Figure 6. The central panel shows a clear sinusoidal dependency of the amplitude on the season. This dependency can be described by a 4th order polynomial fit which summer maximum is 63 nT and winter maximum 23 nT, indicating that the amplitude during summer is about 3 times larger than during winter. Finally, the right panel shows that the delay between maximum and consecutive minimum is longer during summer (around 6–7 hr) than during winter (around 5 hr).

For  $x_D$ , the definition of a maximum and minimum (and successively delay and amplitude) during sunlit hours is not applicable. Its trend generally has only one extremum during the day (see Figure 6) which visualisation analog to Figure 8 can be found in Supporting Information S1. The timing of its minimum at CLF shows a distinct shift of approximately 2 hr around equinox (starting around 08 hr LT between spring and summer and around 10 hr LT during autumn and winter) which is comparable to the shift observed in  $y_D$ . The amplitude of the minimum has a similar trend to what is observed for the peak-to-peak amplitude of  $y_D$ : a polynomial fit of order 3 can be used to describe its variations. The summer minimum is around -15 nT and the spring minimum is around -5 nT, indicating that the summer amplitude is 3 times larger than during spring.

Returning to the day-to-day variability of the signal, it is clear from Figure 8 that, for any given  $L_s$ , a spread is observed in all three parameters of interest: local time occurrence of extrema, amplitude and delay for  $y_D$ . This spread is higher during solstices than during equinoxes, and is also doubled during summer with respect to winter. For the amplitude, the standard deviation is 12.17 nT for the summer period ( $45^\circ < L_s < 135^\circ$ ) and 7.8 nT during winter ( $225^\circ < L_s < 315^\circ$ ), suggesting that the spread during summer increases by over 60% compared to winter. For  $x_D$  amplitude, the standard deviation, however, is rather constant, with maximum differences of 20%.

Overall, we see a total day-to-day variability in amplitude for  $y_D$  of about 20%–30% and for  $x_D$  of about 20%.

## 4. Physical Sources Within the Baseline

In this section, we relate the characteristic variations of the filter outputs, that is, the baseline elements, to sources that are known to contribute to the quiet geomagnetic field.

### 4.1. Secular Variation

The secular variation is the evolution of Earth's intrinsic magnetic field over time that induces a smooth shift within geomagnetic field measurements at stable ground locations. The magnetic pole configuration is such that the magnetic North Pole moves closer to Europe (Olsen & Mandea, 2007) and thus CLF is slowly drifting to higher magnetic latitudes, enhancing the magnetic field intensity at its location. This increase in field strength can be observed in each component of the magnetic field measured at CLF and in particular here in both  $x_{>24}$  and  $y_{>24}$  (see the upper panels of Figure 3). The magnitude of  $y_{>24}$  is lower than that of  $x_{>24}$  as the magnetic meridian is close to geographic North (equal in 2014 when  $Y = 0$  and thus declination was zero at that point). Furthermore,  $y_{>24}$  shows less short-time variability than  $x_{>24}$ , as it is proportionally less affected by fluctuations from external sources. The observed 27-day variation is in agreement with Briggs (1984) and Van De Kamp (2013) who attribute these to either the solar rotation period or tidal variations that arise from the interaction between solar-quiet and lunar tides. However, we cannot exclude the possibility that these variations are a superposition of sources enhancing each other within the same frequency range. Here we would like to point out, that signatures of geomagnetic storms are identifiable within the long-term filters. For example, the famous Halloween storms in 2003 can be clearly identified in both,  $x_{>24}$  and  $y_{>24}$ .

### 4.2. Seasonal and Local Time Patterns of the Quiet Daily Variations

The analysis presented in Figure 6 is in good agreement with the magnetic footprints one expects from the solar quiet current cells flowing at an altitude of about 110 km above the magnetic observatories, that is, the increase of activity at sunrise, the inversion of the  $x_D$  variations for locally close observatories (e.g., CLF vs. SFS, ASP vs. CNB) and the inversion of the  $y_D$  variations between observatories located in different hemispheres (e.g., CLF vs. CNB). This implies that the combined filter output from the 24, 12, 8 and 6 hr filters are the major contributors to the Sq currents.

While the overall day-side patterns of  $x_D$  and  $y_D$  are clearly related to the Sq currents, some specific details in Figure 6 demand further discussion. When useful and applicable, we refer to additional stations which can be found in Supporting Information S1. First,  $x_D$  of CLF and CNB, and to a lesser extent  $y_D$ , show some remnant activity in the night-side, which is in contrast to stations located closer to the equator (SFS and ASP). This feature is also observed for stations over Northern America and Northern Asia (see Supporting Information S1). The night-side enhancements may be related to the closer proximity of the stations to the auroral electrojets. These currents essentially flow azimuthally (i.e., affecting mainly the magnetic X component), increasing in intensity during summer and are modulated by substorm activity with recurrence rates of about 2–4 hr (Smith et al., 2017). Nevertheless, the level of night-side activity remains generally very weak (below 5 nT), as expected for quiet days. For disturbed days, this activity is enhanced as seen on Figures 4 and 5.

On the day-side,  $y_D$  is remarkably stable from one station to the other, having opposite signs between hemispheres. For all stations, the intensification is phased with season, being higher during summer when solar illumination is stronger. The activity follows the local sunrise smoothly, but decreases drastically before sunset, around 15 hr LT, at least in NH. While it is easy to understand that solar illumination is the primary factor triggering the Sq current flow by enhancing locally neutral winds and electron density, it is less evident why the current should decrease before sunset. As for the neutral atmosphere, we looked at various critical parameters given by empirical state-of-the-art models during the same very quiet periods, such as neutral winds (HWM-14, see Drob et al. (2015)), neutral densities, temperature and pressure (NRLMSISE-00, see Picone et al. (2002)). No relationship between the variations of these parameters and the observed constant decrease around 15 hr LT was evident. This analysis was conducted with empirical models which may explain the difficulty to correlate the Sq magnetic variations with thermospheric parameters. More investigations on this topic are necessary and could invoke some kind of saturation of the atmosphere.

Whereas  $y_D$  has a clear pattern,  $x_D$  shows a more complex day-side behaviour. The  $X$  component of the Sq current, and thus the  $x_D$  filter, indicates the position of the observatory with respect to the current cell's focus location. For an ideal current cell with a circular shape, a negative (positive)  $x_D$  component indicates that the station is located above (below) the focus. When  $x_D$  is close to zero, the station is beneath the cell's focus. A stable pattern with smooth variations in  $x_D$  (apart from the expected decrease of the activity during winter when solar illumination decreases) is observed for stations located far of the Sq current cell focus (for examples see Supporting Information S1 SEA for: MMB and PHU over Asia, FRD and SJG over North America, WNG and GUI over Europe, KDU over Australia). However, stations South of the Sq current focus in Europe show less smooth and stable patterns with respect to SJG and PHU. This may be related to the tilted position of the magnetic equator, deforming the southern part of the Sq cell. Stations close to the Sq cell focus show a more complex pattern, particularly for CLF, SFS (and KNY in Supporting Information S1) in NH and ASP and CNB in SH. First, the overall  $x_D$  component is weaker, confirming the proximity of the Sq cell focus. Second, variations of the minimum/maximum of  $x_D$  in local time with respect to season reflects variations either of the Sq focus position and/or of the Sq cell shape and size (Stening, 2008; Stening et al., 2007).

As shown by Yamazaki et al. (2011), the local time of the cell's focus shifts to earlier times during summer compared to winter months, which is in agreement with the morning shift of the minimum occurrence of  $x_D$  observed at CLF and CNB (see blue feature of  $x_D$  in Figure 6), situated at slightly higher latitudes than the Sq focus. CLF is closer to this Sq focus than CNB, as its minimum almost disappears during winter. This may be an indication that the Sq focus also moves to higher latitudes during winter and that the Sq cell almost disappears (which is in agreement with Soloviev et al. (2019)). This behaviour is also confirmed at SFS, when between summer and fall equinox, a minimum is followed by a maximum, showing that the Sq focus is likely to be very close to SFS and moves from above to beneath the focus during the course of a day, as proposed by Anad et al. (2016). This behaviour is also seen at KNY and less clearly at TUC (see Supporting Information S1). The  $x_D$  component at ASP behaves similarly to SFS, but presumably never crosses the Sq focus during summer, since no real minimum is observed during morning hours.

A last intriguing feature is observed in  $y_D$  just before sunrise during local winter, when a local minimum is observed at CLF and SFS and a local maximum at ASP and CNB (see again Figure 6). This behaviour is difficult to explain from the Sq current cell system alone. Considering the possibility of inter-hemispheric field-aligned-currents (IHFACs), as analysed by for example, Olsen (1997) and Park et al. (2011), such currents should flow at dawn. As Shinbori et al. (2017) stated, the  $Y$  component of the magnetic field is the most susceptible to be perturbed by the presence of IHFACs. Thus, this local minimum/maximum before sunrise could encompass magnetic variations associated with such dawn IHFACs. The dawn minimum is fainter above North America (see Supporting Information S1), which is consistent with the findings of Lühr et al. (2015), that IHFACs are more intense above Europe and almost disappear above North America. Again, the level of activity of this feature is low. The  $x_D$  component also has a local maximum centred just after sunrise during local winter at ASP, SFS, CNB (and KNY). The cause of this structure still remains unclear but may also be related to such IHFACs.

Overall, it is clear from this section that  $x_D$  and  $y_D$  capture the Sq current cell properties well.

#### 4.3. Day-To-Day Variability

Figures 7 and 8 demonstrate a non-negligible day-to-day variability of the combined filter outputs  $x_D$  and  $y_D$  which is more pronounced during summer. This phenomenon has been observed in the majority of physical and electro-dynamical parameters of the ionosphere for more than 40 years and is well documented for Sq currents in the literature (see e.g., Brown and Williams (1969); Greener and Schlapp (1979); Schlapp (1968); Takeda (1984); Yamazaki and Maute (2016)). Simulations from Yamazaki et al. (2016) showed that variations within the Sq current can be attributed to 75% to solar illumination and to 25% to atmospheric and magnetospheric drivers. Forbes et al. (2000) found that around 25%–30% of the plasma peak density variations in the 1–2 hr to days range in the F-region can be attributed to meteorological phenomena. The day-to-day variabilities found in our study are in the order of 20%–30% for the amplitude of  $x_D$  and  $y_D$ , which is consistent with these previous studies. Additionally, the results presented in Figure 8 reveal two intriguing properties of the day-to-day variability:

- The occurrence in local time of the maxima and minima, as well as the delay among them has a clear dependency on season.

- The spread of the amplitude is clearly dependent on season.

Our analysis minimises magnetospheric influences by taking into account only very quiet magnetic conditions. However, on such quiet days, solar flares may still occur and disturb the signal. To investigate on this, we excluded all quiet days on which X and M class solar flares were recorded during daylight hours and re-ran our analysis. Expectably, the percentages of day-to-day variability did not change significantly. Flares can have very strong effects on the ionospheric ionization and thus on the associated currents, but their influences are only present for a very limited time (Liu et al., 1996).

These considerations lead us to conclude that the majority of the observed day-to-day variability may be attributed to atmospheric drivers only, which underlying processes become stronger with increasing solar illumination, confirming the neutral atmosphere as a key role.

Gravity waves and tides within the neutral atmosphere are known to exhibit complex interference behaviour that can drastically change from 1 day to another (Liu et al., 2018; Stening et al., 2005). For example, the lunar tide induced by the revolution of the moon around Earth has a period of 12.4 hr which is very close to that of the solar semi-diurnal one. The small difference in period may lead to a smooth drift of the contributions of  $x_D$  and  $y_D$ , leading to amplification or reduction of the global signal over a course of a few days. Attempts to model such a lunar tide effect did not reproduce the variations of amplitude within the combined daily contributions  $x_D$  and  $y_D$ . This tends to conclude that several sources of tides and waves are involved in this phenomenon which remains challenging to model.

## 5. Comparison of Baselines During Magnetically Quiet Days

On days without major external influences, the magnetic field measurements follow regular daily variations that Bartels et al. (1939) describes as a to-be-expected smooth curve which philosophy persists till the present day. This definition implies that there is no quantitative way to evaluate the performance of baselines. We can, however, compare our baseline with existing and widely accepted counterparts like the FMI method and SuperMAG method. The mentioned PC index and IMAGE methods are designed for polar stations and auroral Scandinavian magnetometers respectively and thus are out of range for low- and mid-latitudes considered in this work.

To determine the baseline, the FMI method performs a 5th degree harmonic fit to hourly means, which are determined taking into account apriori information such as magnetic latitude and local time (Sucksdorff et al., 1991). The original software written in C is made available through the long-term ISGI repository. The method used by the SuperMAG service consists of determining its own field orientation, followed by a daily baseline, annual trend and residual offset that differs for each of the magnetic field vector components (Gjerloev, 2012). Their baseline data is not directly accessible and several steps had to be executed to make them available for this work. SuperMAG provides the actual and baseline removed data in a magnetic local frame that uses an arbitrary declination. In order to compare them to the original data as provided by observatories from INTERMAGNET, SuperMAG data needs to be transformed to the local geographic frame first, followed by subtracting the baseline removed data from the measurements in order to retrieve the baseline. Hereafter we compare our method to the FMI method, referred to as  $x_K, y_K$ ; and to the SuperMAG method, referred to as  $x_S, y_S$ . As such, Figure 9 demonstrates our baseline (red) in comparison with the  $X, Y$  components (grey), the FMI (blue) and the SuperMAG (green) baselines, whereby grey shaded time intervals indicate non-CK48 days.

During magnetically quiet days (white background), our and FMI baselines closely follow the magnetic activity, capturing the day-to-day variability smoothly and showing little discrepancies between them. The SuperMAG baseline  $x_S, y_S$  shows some distinct differences, especially for the  $X$  component. The actual measurements are not always followed closely, for example, there is a clear positive and negative offset between the magnetic observatory data and SuperMAG estimation of the quiet baseline for the  $X$  component during the afternoon/night of 10 and 13th December. In general, the SuperMAG method follows a rather steady pattern showing minor differences from 1 day to another. As shown before, there is a non-negligible day-to-day variation within the signal, which is most likely induced by atmospheric drivers. These variations are well captured by  $x_B, y_B$  and  $x_K, y_K$ , but less with  $x_S, y_S$  indicating that it may tend to overestimate magnetospheric drivers during quiet days. To be able to qualitatively compare baselines, we calculate the difference between ours and each of the two other methods for all CK48 days of 2009. We make the simple assumption that this difference can be described by a Gaussian

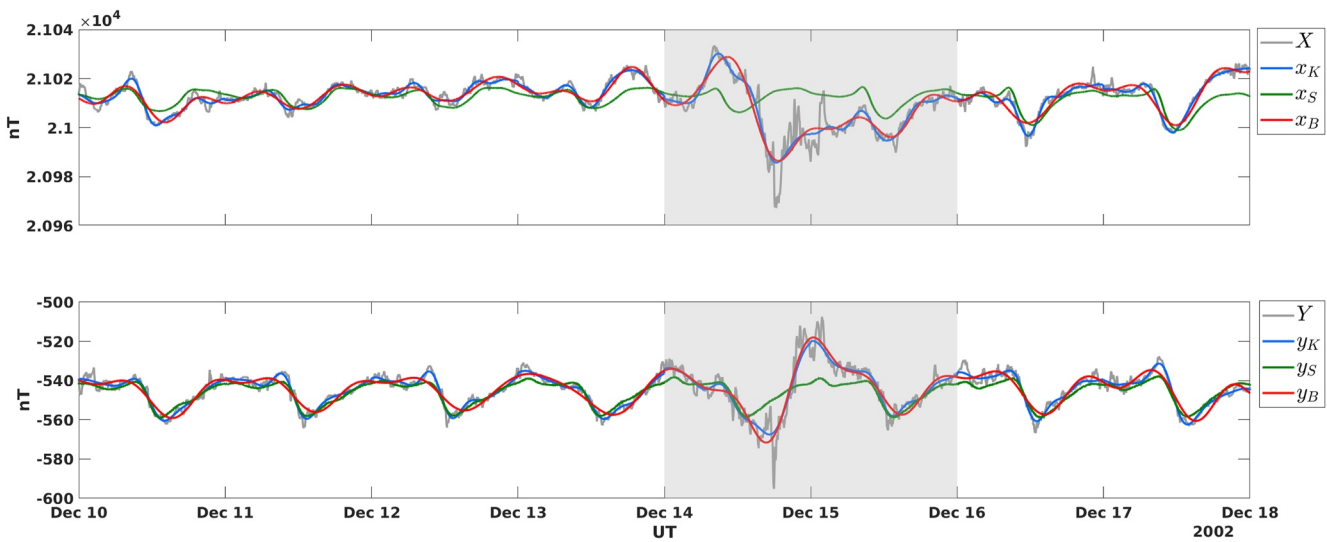


**Figure 9.** Comparison of baseline methods. The methods of the introduced baseline (red), Finnish Meteorological Institute (blue) and SuperMAG (green) for  $X$ ,  $Y$  components (grey) at Chambon-la-Forêt during winter 2002 are presented. The grey shaded areas indicate non-CK48 days.

distribution, using its variance to quantify deviations. For the  $X$  component, we find a variance of 1.6 nT, and for the  $Y$  component 1.7 nT between our baselines and the FMI ones; and 6.2 nT, and 4.6 nT between our baselines and SuperMAG ones. This implies that our determination of baselines can be used instead of the FMI method without causing major changes in the baseline reconstruction during magnetically quiet days. Additionally, the filtering method produces baselines without any further information than the magnetic measurements themselves, whereas the FMI method needs the magnetic latitude as an input, which is evolving over time and not trivial to be determined in real-time. This property gives the filtering method the main advantage of being directly applicable, that is, as soon as the geomagnetic field data is available.

Giving a detailed analysis of our filtering method during disturbed magnetic periods would far exceed the scope of the present paper. However, we would like to add a few thoughts on the application of our method during non-quiet days. During non-CK48 days, indicated by the grey shaded area in Figure 9, clear differences between all three baseline methods are evident. Our filter method follows the activity very closely, including the depression and the following fluctuations on 14th December. These features are followed to a lesser extend by the FMI method. Contrarily, the SuperMAG baseline is insensitive to any of these storm effects in this example and follows a smooth curve from the last quiet day to the next quiet day. This may suggest that our filter and the FMI methods underestimate, whereas the SuperMAG may overestimate the actual storm activity and its effects. The implication for our filter approach is, that it is not directly applicable during disturbed periods, and thus quiet and storm time need to be treated separately (which is true for the SuperMAG and IMAGE methods as well). The discrimination between quiet and disturbed periods may be done by statistical measures, as has been done by Gjerloev (2012) and Van De Kamp (2013), and by additionally taking into account dependencies on season or solar activity. Furthermore, the fact that there is no quantitative way to validate quiet curves remains especially true during storm times. For example, in Figure 9 the SuperMAG baselines  $x_s$  and  $y_s$  during the two disturbed days are very similar to their quiet curve of the preceding day, which can be interpreted physically as a fully developed Sq current cell. However such a full system does not necessarily form during a disturbance event (Le Huy & Amory-Mazaudier, 2008) which may be even the case in this example, as the actual measurements are very different from the expected Sq current signature.

Another important observation is that signatures of storms, are also contained within the long-term filter as described in Section 4.2. This shows that all level of filters can be strongly modified during non-quiet periods, making our filter baseline not directly applicable outside quiet periods.

Future work will address the application of our filter method baseline for magnetically disturbed periods, focusing on the aforementioned considerations.

## 6. Conclusion

This paper introduces a method to directly determine baselines of geomagnetic field measurements during magnetically quiet periods in low- and mid-latitudinal regions. The method is based upon signal filtering techniques to extract long-term (with periods above 36 hr) and (sub-) diurnal (with periods of 24, 12, 8 and 6 hr) variations within the time-series of each magnetic component.

We conducted an exhaustive analysis of the contribution's variations, relating it to physical sources that are known to constitute the quiet geomagnetic field. The long-term filter includes the contributions induced by the secular variation, as well as tidal effects. The combined diurnal contributions have a strong dependency on local time and season and show the typical day-to-day variability which lets us confirm that the Sq current system is strongly modified by the underlying atmosphere. Furthermore, the results for the day-to-day variability as extracted by the filtering technique suggest that the amplitude and its spread around an expected value, as well as the occurrence of extrema, have a clear seasonal dependency. The filtering technique provides promising preliminary results and may be used for more thorough analysis of quiet Sq current systems in future works.

The baseline is then made up of the superposition of the long-term and the combined daily contributions. During magnetically quiet conditions our filter baseline smoothly follows the variations in the X and Y component. It produces remarkably similar baselines as the ones calculated with the FMI method with the advantage of not needing apriori information. We conclude that our approach characterises the quiet magnetic field well and is suitable to be used during magnetically quiet periods. The filtering method tends to follow the activity very closely, risking to under-estimate potential storm effects and thus is not directly applicable during magnetically disturbed periods.

As the introduced filtering method is a standard signal-treatment approach that does not need any apriori information for its application, it is directly applicable to any magnetic observatory in low and mid-latitudes independent of the time period. Therefore, the limiting factor for its real-time application is the discrimination of quiet versus non-quiet periods and the determination of the baseline during non-quiet periods. Once these challenges are overcome, it has the capability of being used in (near) real-time applications that make use of low- and mid-latitude magnetic observatories, like space weather severeness estimations and index derivations.

## Acknowledgments

The results presented in this paper rely on: (a) data collected at magnetic observatories. We thank the national institutes that support them and INTERMAGNET (International Real-time Magnetic Observatory Network) for promoting high standards of magnetic observatory practice ([www.intermagnet.org](http://www.intermagnet.org)). (b) Magnetic activity indices, and related data products, calculated and made available by ISGI (International Service of Geomagnetic Indices) Collaborating Institutes from data collected at magnetic observatories. We thank the involved national institutes and ISGI ([www.isgi.unistra.fr](http://www.isgi.unistra.fr)). This work was supported by the PNST (*Programme National Soleil Terre*), from CNRS-INSU (*Institut des Sciences de l'Univers* of *Centre National de la Recherche Scientifique*) co-funded by CNES (*Centre National d'Etudes Spatiales*) and CEA (*Commissariat à l'Energie Atomique et aux Energies Alternatives*), and by TOSCA committee from CNES focused on Space weather and Geomagnetism. This work was supported by CNES. Veronika Haberle is sponsored by Thales Alenia Space, Toulouse. The authors acknowledge the support of the French ANR (*Agence Nationale de la Recherche*), under grant ANR-20-ASTC-0030 (project ASTRID PRISMS).

## Data Availability Statement

The magnetic observatory data are available from INTERMAGNET data repository: <http://doi.org/10.17616/R3XK82>. The magnetic activity indices are available from ISGI data repository: <http://doi.org/10.17616/R3WS49>.

## References

- Anad, F., Amory-Mazaudier, C., Hamoudi, M., Bourouis, S., Abtou, A., & Yizengaw, E. (2016). Sq solar variation at Medea Observatory (Algeria), from 2008 to 2011. *Advances in Space Research*, 58(9), 1682–1695. <https://doi.org/10.1016/j.asr.2016.06.029>
- Bartels, J., Heck, N. H., & Johnston, H. F. (1939). The three-hour-range index measuring geomagnetic activity. *Journal of Geophysical Research*, 44(4), 411. <https://doi.org/10.1029/TE044I004P00411>
- Behannon, K. W., & Ness, N. F. (1966). *The design of numerical filters for geomagnetic data analysis (NASA Technical Note No. NASA-TN-D-3341)*. Goddard Space Flight Center NASA.
- Behannon, K. W., & Ness, N. F. (1966). Magnetic storms in the earth's magnetic tail. *Journal of Geophysical Research*, 71(9), 2327–2351. <https://doi.org/10.1029/JZ071I009P02327>
- Bhargava, B. N., & Yacob, A. (1970). The secular variation of the magnetic field and its cyclic components. *Journal of Atmospheric and Terrestrial Physics*, 32(3), 365–372. [https://doi.org/10.1016/0021-9169\(70\)90008-5](https://doi.org/10.1016/0021-9169(70)90008-5)
- Briggs, B. (1984). The variability of ionospheric dynamo currents. *Journal of Atmospheric and Terrestrial Physics*, 46(5), 419–429. [https://doi.org/10.1016/0021-9169\(84\)90086-2](https://doi.org/10.1016/0021-9169(84)90086-2)
- Brown, G., & Williams, W. (1969). Some properties of the day-to-day variability of Sq (H). *Planetary and Space Science*, 17(3), 455–470. [https://doi.org/10.1016/0032-0633\(69\)90076-2](https://doi.org/10.1016/0032-0633(69)90076-2)
- Campbell, W. H. (1989). An introduction to quiet daily geomagnetic fields. *Pure and Applied Geophysics*, 131(3), 315–331. <https://doi.org/10.1007/BF00876831>
- Campbell, W. H. (2003). *Introduction to geomagnetic fields*. Cambridge University Press. <https://doi.org/10.1017/cbo9781139165136>
- Cliver, E. W., & Dietrich, W. F. (2013). The 1859 space weather event revisited: Limits of extreme activity. *Journal of Space Weather and Space Climate*, 3, A31. <https://doi.org/10.1051/SWSC/2013053>
- Constable, C. G., & Constable, S. C. (2004). Satellite magnetic field measurements: Applications in studying the deep Earth. In *Geophysical monograph series* (Vol. 150, pp. 147–159). Blackwell Publishing Ltd. <https://doi.org/10.1029/150GM13>
- Drob, D. P., Emmert, J. T., Meriwether, J. W., Makela, J. J., Doornbos, E., Conde, M., et al. (2015). An update to the Horizontal Wind Model (HWM): The quiet time thermosphere. *Earth and Space Science*, 2(7), 301–319. <https://doi.org/10.1002/2014EA000089>

- Finlay, C. C., Lesur, V., Thébault, E., Vervelidou, F., Morschhauser, A., & Shore, R. (2017). Challenges handling magnetospheric and ionospheric signals in internal geomagnetic field modelling. *Space Science Reviews*, 206(1), 157–189. <https://doi.org/10.1007/s11214-016-0285-9>
- Forbes, J. M., Palo, S. E., & Zhang, X. (2000). Variability of the ionosphere. *Journal of Atmospheric and Solar-Terrestrial Physics*, 62(8), 685–693. [https://doi.org/10.1016/S1364-6826\(00\)00029-8](https://doi.org/10.1016/S1364-6826(00)00029-8)
- Gjerloev, J. W. (2012). The SuperMAG data processing technique. *Journal of Geophysical Research*, 117(A9), 9213. <https://doi.org/10.1029/2012JA017683>
- Greener, J. G., & Schlapp, D. M. (1979). A study of day-to-day variability of Sq over Europe. *Journal of Atmospheric and Terrestrial Physics*, 41(2), 217–223. [https://doi.org/10.1016/0021-9169\(79\)90014-X](https://doi.org/10.1016/0021-9169(79)90014-X)
- Hitchman, A. P., Lilley, F. E. M., & Campbell, W. H. (1998). The quiet daily variation in the total magnetic field: Global curves. *Geophysical Research Letters*, 25(11), 2007–2010. <https://doi.org/10.1029/98GL51332>
- Jadhav, G., Rajaram, M., & Rajaram, R. (2002). A detailed study of equatorial electrojet phenomenon using Ørsted satellite observations. *Journal of Geophysical Research*, 107(A8), 12–1. <https://doi.org/10.1029/2001JA000183>
- Janzhura, A., & Troshichev, O. (2008). Determination of the running quiet daily geomagnetic variation. *Journal of Atmospheric and Solar-Terrestrial Physics*, 70(7), 962–972. <https://doi.org/10.1016/j.jastp.2007.11.004>
- Kozyreva, O. V., Pilipenko, V. A., Belakovsky, V. B., & Sakharov, Y. A. (2018). Ground geomagnetic field and GIC response to March 17, 2015, storm. *Earth Planets and Space*, 70(1), 1–13. <https://doi.org/10.1186/S40623-018-0933-2>
- Kunagu, P., Balasis, G., Lesur, V., Chandrasekhar, E., & Papadimitriou, C. (2013). Wavelet characterization of external magnetic sources as observed by CHAMP satellite: Evidence for unmodelled signals in geomagnetic field models. *Geophysical Journal International*, 192(3), 946–950. <https://doi.org/10.1093/GJI/GGS093>
- Laundal, K. M., & Richmond, A. D. (2016). Magnetic coordinate systems. *Space Science Reviews*, 206(1–4), 27–59. <https://doi.org/10.1007/s11214-016-0275-y>
- Le Huy, M., & Amory-Mazaudier, C. (2008). Planetary magnetic signature of the storm wind disturbance dynamo currents:  $D_{dyn}$ . *Journal of Geophysical Research*, 113(2). <https://doi.org/10.1029/2007JA012686>
- Liu, H. L., Bardeen, C. G., Foster, B. T., Lauritzen, P., Liu, J., Lu, G., et al. (2018). Development and validation of the Whole Atmosphere Community Climate Model with thermosphere and ionosphere extension (WACCM-X 2.0). *Journal of Advances in Modeling Earth Systems*, 10(2), 381–402. <https://doi.org/10.1029/2017MS001232>
- Liu, J. Y., Chiu, C. S., & Lin, C. H. (1996). The solar flare radiation responsible for sudden frequency deviation and geomagnetic fluctuation. *Journal of Geophysical Research*, 101(A5), 10855–10862. <https://doi.org/10.1029/95JA03676>
- Lühr, H., Kervalishvili, G., Michaelis, I., Rauberg, J., Ritter, P., Park, J., et al. (2015). The interhemispheric and F region dynamo currents revisited with the Swarm constellation. *Geophysical Research Letters*, 42(9), 3069–3075. <https://doi.org/10.1002/2015GL063662>
- Ma, R., Xu, J., Wang, W., & Lei, J. (2012). The effect of 27 day solar rotation on ionospheric F2 region peak densities ( $N_m F_2$ ). *Journal of Geophysical Research*, 117(A3), 3303. <https://doi.org/10.1029/2011JA017190>
- Mayaud, P.-N. (1967). *Atlas of K Indices* (vol. IAGA bull No. 21). IUGG Publication Office.
- Mayaud, P.-N. (1972). The aa indices: A 100-year series characterizing the magnetic activity. *Journal of Geophysical Research*, 77(34), 6870–6874. <https://doi.org/10.1029/JA077I034P06870>
- Menvielle, M., Iyemori, T., Marchaudon, A., & Nosé, M. (2011). *Geomagnetic observations and models*. Springer Netherlands. <https://doi.org/10.1007/978-90-481-9858-0>
- Menvielle, M., Papitashvili, N., Häkkinen, L., & Sucksdorff, C. (1995). Computer production of K indices: Review and comparison of methods. *Geophysical Journal International*, 123(3), 866–886. <https://doi.org/10.1111/J.1365-246X.1995.TB06895.X>
- Ness, N. F., & Williams, D. J. (1966). Correlated magnetic tail and radiation belt observations. *Journal of Geophysical Research*, 71(1), 322–325. <https://doi.org/10.1029/JZ071I001P00322>
- Olsen, N. (1997). Ionospheric F region currents at middle and low latitudes estimated from Magsat data. *Journal of Geophysical Research*, 102(A3), 4563–4576. <https://doi.org/10.1029/96JA02949>
- Olsen, N., & Mandea, M. (2007). Will the magnetic North Pole move to Siberia? *Eos, Transactions American Geophysical Union*, 88(29), 293. <https://doi.org/10.1029/2007EO290001>
- Park, J., Lühr, H., & Min, K. W. (2011). Climatology of the inter-hemispheric field-aligned current system in the equatorial ionosphere as observed by CHAMP. *Annales Geophysicae*, 29(3), 573–582. <https://doi.org/10.5194/angeo-29-573-2011>
- Picone, J. M., Hedin, A. E., Drob, D. P., & Aikin, A. C. (2002). NRLMSISE-00 empirical model of the atmosphere: Statistical comparisons and scientific issues. *Journal of Geophysical Research*, 107(A12), 15–1. <https://doi.org/10.1029/2002JA009430>
- Proakis, J., & Manolakis, D. (2006). *Digital signal processing* (4th edn). Pearson.
- Schlapp, D. M. (1968). World-wide morphology of day-to-day variability of Sq. *Journal of Atmospheric and Terrestrial Physics*, 30(10), 1761–1776. [https://doi.org/10.1016/0021-9169\(68\)90096-2](https://doi.org/10.1016/0021-9169(68)90096-2)
- Shinbori, A., Koyama, Y., Nosé, M., Hori, T., & Otsuka, Y. (2017). Characteristics of seasonal variation and solar activity dependence of the geomagnetic solar quiet daily variation. *Journal of Geophysical Research: Space Physics*, 122(10), 796–10. <https://doi.org/10.1002/2017JA024342>
- Shinbori, A., Koyama, Y., Nose, M., Hori, T., Otsuka, Y., & Yatagai, A. (2014). Long-term variation in the upper atmosphere as seen in the geomagnetic solar quiet daily variation. *Earth Planets and Space*, 66(1), 1–20. <https://doi.org/10.1186/S40623-014-0155-1>
- Smith, A. R., Beggan, C. D., Macmillan, S., & Whaler, K. A. (2017). Climatology of the auroral electrojets derived from the along-track gradient of magnetic field intensity measured by POGO, Magsat, CHAMP, and Swarm. *Space Weather*, 15(10), 1257–1269. <https://doi.org/10.1002/2017SW001675>
- Soloviev, A., Smirnov, A., Gvishiani, A., Karapetyan, J., & Simonyan, A. (2019). Quantification of Sq parameters in 2008 based on geomagnetic observatory data. *Advances in Space Research*, 64(11), 2305–2320. <https://doi.org/10.1016/J.ASR.2019.08.038>
- Stening, R. (2008). The shape of the Sq current system. *Annales Geophysicae*, 26(7), 1767–1775. <https://doi.org/10.5194/angeo-26-1767-2008>
- Stening, R., Reztsova, T., & Le Huy, M. (2005). Day-to-day changes in the latitudes of the foci of the Sq current system and their relation to equatorial electrojet strength. *Journal of Geophysical Research*, 110(A10), A10308. <https://doi.org/10.1029/2005JA011219>
- Stening, R., Reztsova, T., & Le Huy, M. (2007). Variation of Sq focus latitudes in the Australian/Pacific region during a quiet sun year. *Journal of Atmospheric and Solar-Terrestrial Physics*, 69(6), 734–740. <https://doi.org/10.1016/j.jastp.2006.12.002>
- Sucksdorff, C., Pirjola, R., & Häkkinen, L. (1991). Computer production of K-indices based on linear elimination. *Geophysical Transactions*, 36(3–4), 333–345.
- Takeda, M. (1984). Day-to-day variation of equivalent sq current system during March 11–26, 1970. *Journal of Geomagnetism and Geoelectricity*, 36(5), 215–228. <https://doi.org/10.5636/jgg.36.215>
- Takeda, M. (1999). Time variation of global geomagnetic Sq field in 1964 and 1980. *Journal of Atmospheric and Solar-Terrestrial Physics*, 61(10), 765–774. [https://doi.org/10.1016/S1364-6826\(99\)00028-0](https://doi.org/10.1016/S1364-6826(99)00028-0)

- Tapping, K. F. (2013). The 10.7 cm solar radio flux (F10.7). *Space Weather*, 11(7), 394–406. <https://doi.org/10.1002/swe.20064>
- Van De Kamp, M. (2013). Harmonic quiet-day curves as magnetometer baselines for ionospheric current analyses. *Geoscientific Instrumentation, Methods and Data Systems*, 2(2), 289–304. <https://doi.org/10.5194/GI-2-289-2013>
- Wardinski, I., & Thébault, E. (2019). Modelling internal and external geomagnetic fields using satellite data. *Geomagnetism, Aeronomy and Space Weather: A Journey from the Earth's Core to the Sun*, 84–97. <https://doi.org/10.1017/9781108290135.008>
- Yamazaki, Y., Häusler, K., & Wild, J. A. (2016). Day-to-day variability of midlatitude ionospheric currents due to magnetospheric and lower atmospheric forcing. *Journal of Geophysical Research: Space Physics*, 121(7), 7067–7086. <https://doi.org/10.1002/2016JA022817>
- Yamazaki, Y., & Maute, A. (2016). Sq and EEJ—A review on the daily variation of the geomagnetic field caused by ionospheric dynamo currents. *Space Science Reviews*, 206(1–4), 299–405. <https://doi.org/10.1007/s11214-016-0282-z>
- Yamazaki, Y., Yumoto, K., Cardinal, M. G., Fraser, B. J., Hattori, P., Kakinami, Y., et al. (2011). An empirical model of the quiet daily geomagnetic field variation. *Journal of Geophysical Research*, 116(A10), 10312. <https://doi.org/10.1029/2011JA016487>